Euler-Lagrange CFD modelling of unconfined gas mixing in anaerobic digestion

Davide Dapelo[a,*], Federico Alberini[b], John Bridgeman[a]

[a] University of Birmingham, School of Civil Engineering, Birmingham B15 2TT, United Kingdom
[b] University of Birmingham, School of Chemical Engineering

Abstract

A novel Euler-Lagrangian (EL) computational fluid dynamics (CFD) finite volume-based model to simulate the gas mixing of sludge for anaerobic digestion is developed and described. Fluid motion is driven by momentum transfer from bubbles to liquid. Model validation is undertaken by assessing the flowfield in a labscale model with particle image velocimetry (PIV). Conclusions are drawn about the upscaling and applicability of the model to full-scale problems, and recommendations are given for optimum application.

Keywords: CFD, Euler-Lagrangian, Anaerobic digestion, Non-Newtonian fluid, Gas mixing, PIV

[Table 1 about here.]

1. Introduction

Through the production of biogas, anaerobic digestion is one of the most technically-mature and cost-effective processes for sustainable energy production and management of sludges from livestock facilities, municipal solid waste and wastewater treatment plants.

*Corresponding author.
Tel.: +44 (0) 121 414 5145
Email: dxd265@bham.ac.uk

A key component for the success of an anaerobic digestion plant is mixing: proper mixing ensures uniformity of temperature, enables colonies of bacteria to digest the material entering the digester evenly, and prevents the formation of surface crusts. However, mixing is generally an energy intensive operation, with approximately 20% of the total energy input of digesters absorbed by mixing (Bridgeman, 2012). For this reason, mixing should be optimized in order to optimize biogas production. In this sense, optimization seeks the minimum degree of mixing in order to save energy, without compromising, and indeed enhancing, biogas production.

Although the importance of thorough mixing has always been recognised, recent studies, both traditional (Stroot et al., 2001; McMahon et al., 2001; Ong et al., 2002; Gómez et al., 2006; Ward et al., 2008) and CFD-based (Bridgeman, 2012; Wu, 2012), point out that an excess of mixing can have a detrimental effect both on the economics of an anaerobic digestion plant and on the process of digestion itself.

The two main mixing methods are: mechanical mixing and gas mixing. The former employs impellers to stir the sludge; whereas in the latter, biogas is taken from the top of the tank and pumped into the sludge through a series of nozzles. The bubbles rise in columns via buoyancy and transfer momentum to the surrounding sludge. This momentum transfer takes place due to the push force that the bubbles exert to the surrounding liquid, and the riptide effect arising from the low-pressure region created by the motion of the bubbles.

Thanks to the progress of computer performance, computational fluid dynamics (CFD) has become an invaluable resource in the simulation of processes involving fluid flow and heat transfer. However, while a lot of work has been done to understand mechanical mixing of sludge in anaerobic digestion, gas mixing still remains poorly studied. During the gas-mixing process, a complex pattern of momentum exchange between bubbles and liquid phase takes place, and therefore a

genuine multiphase model is required to reproduce the liquid phase mixing robustly and with fidelity. However, to our knowledge, only Vesvikar and Al-Dahhan (2005); Wu (2010, 2012) have investigated this subject with a robust multiphase model. Karim et al. (2007) investigated gas mixing, but they carried out broad simplifications in their analysis, as their model works only on a specific case of draft tube-driven mixing. Furthermore, the effect of gas injection was modelled by specifying the outlet velocity at the exit of the draft tube, while the inside the draft tube were not studied. As can be seen, their analysis was actually carried out with a single-phase model: even though their model was able to reproduce the experimental data satisfactorily, it was specific for a very definite problem. Vesvikar and Al-Dahhan (2005) investigated gas mixing in a lab-scale digester with a Euler-Euler two-way-coupling model; Wu (2010, 2012) performed extensive studies by expanding this model to non-Newtonian liquid phases, by comparing the outcome of the model for a broad set of turbulent models, and by integrating the fluid dynamics with a biochemical model.
There is not a universal multiphase model that is optimal to every application (Andersson et al., 2012) – different approaches are possible, each with specific advantages and disadvantages. The Euler-Euler model can handle very complex flows, and this is one of the reasons why it has been largely employed. However, a quantity of empirical information is needed in order to close the momentum equations (Andersson et al., 2012), whereas the Euler-Lagrange model requires a much smaller amount of modelling for closure. For this reason, if the particle number is not too high and the computational expense remains acceptable, the Euler-Lagrangian model provides an attractive alternative. However, no Euler-Lagrange finite volume-based model has been proposed in the literature to simulate gas mixing in anaerobic digestion. Sungkorn et al. (2011) studied highly turbulent constant-viscosity column bubbly flow, while Sungkorn et al. (2012) modelled a generic shear-thinning aerated

stirred tank. However, they did not attempt to reproduce the rheologic characteristics of sludge and, most significantly, they adopted a Lattice-Boltzmann scheme, that is a completely different framework from finite volume. In the finite volume scheme, the fluid is modelled as a continuum, and the aim is to solve the Navier-Stokes equations for the Eulerian velocity $\mathbf{u}(\mathbf{x}, t)$ and pressure $p(\mathbf{x}, t)$ fields. The discretization is carried out by dividing the domain into cells and defining the velocity and pressure fields at the centre of each cell. The Navier-Stokes equations are discretized by applying the Gauss theorem at each cell, and using different discretization schemes in order to interpolate the values of the fields at the cell borders. The numerical solution is carried out with an iterative procedure that solves in turn the momentum Navier-Stokes equation and a Poisson equation for the pressure derived from the Navier-Stokes and the mass conservation equations, using the solution of one as a starting guess for the others until convergence is achieved. In the Lattice-Boltzmann scheme, the fluid is modelled as an ensemble of particles to be treated statistically, and is described by the probability density function $f(\mathbf{x}, \mathbf{v}, t)$ of finding a particle of velocity comprised between $\mathbf{v}$ and $\mathbf{v} + \mathrm{d}\mathbf{v}$ inside the volume element $(\mathbf{x}, \mathbf{x} + \mathrm{d}\mathbf{x})$ and the time interval $(t, t + \mathrm{d}t)$. The probability density function obeys the Boltzmann equation, which relates its total derivative with a collision operator. Density, velocity and pressure fields are worked out from the probability density function. The discretization is carried out by defining a lattice in which the grid points are linked with unitary velocity vectors. The probability density function is defined at the grid points. Each grid point is linked to its neighbours via velocity direction vectors. In order to obtain a physically meaningful solution, it is crucial to define a grid with a sufficiently rich symmetry group. For each lattice velocity direction, the corresponding probability density function is obtained by evolving it from the previous timestep by using the Boltzmann equation according with the scattering matrix and the deviation of the probability density function from the Maxwell (equilibrium) function. The interested reader can consult literature on finite volume CFD such as Versteeg and Malalasekera 1995; Andersson et al. 2012 and on lattice-Boltzmann Succi 2001; Wolf-Gladrow 2005.

The aim of the work reported in this paper is to propose, develop and validate the first Euler-Lagrange finite volume-based model for investigating gas mixing in anaerobic digestion. Sungkorn et al. (2011, 2012) formulated the hypothesis that the requirement for Euler-Lagrangian models of minimum mesh to bubble size ratio (van Wachem and Almstedt, 2003; Andersson et al., 2012) could be relaxed, and validated it inside the Lattice-Boltzmann framework; in the work reported in this paper, this hypothesis was tested in the finite volume framework. Model validation was performed by comparing model outputs with PIV measurements conducted on a 4 litre laboratory-scale tank. Once the validation has been carried out, it will be possible to apply the model to full-scale modelling in future works. The full-scaling will be expected to be less sensitive than the laboratory-scale application proposed in this work because the mesh size in the former will be expected to be increased and, consequently, the mesh to bubble size ratio will increase as well, thus respecting the requirement stated by van Wachem and Almstedt (2003); Andersson et al. (2012).

2. Material and Methods

2.1. Experimental rig

A 4-litre cylindrical, transparent tank was assembled by gluing a 20 cm diameter, 20 cm long, 3 mm thick plexiglass pipe onto a square support of side 25.5 cm. Care was taken in order to make sure that the plexiglass pipe axis passed through the support centre. The junction was sealed with silicon.

In order to minimize the refraction of the PIV laser beam through the curved plexiglass surface, the cylindrical tank was encased within a plexiglass tank fixed to the square support which was subsequently filled with water. The glass layer was set orthogonal to the PIV camera such that refraction through the water-glass and glass-air interfaces might be neglected.

A simple nozzle arrangement was effected by drilling a 1 mm diameter hole through the axis of a plastic bolt of 10 mm head diameter, 5 mm internal diameter, 25 mm length. A hole with the same diameter of the bolt and a compatible threading was drilled at the centre of the squared support. The bolt was screwed through it such that its head remained at the inner side of the support. The bolt head was neglected in the simulations as its size is negligible if compared with the plexiglass pipe. A sketch of the tank is depicted in Figure 1.

[Figure 1 about here.]

The air flow was generated by a Nitto Kohki Co., LTD LA-28B air compressor and flow rate was controlled between 0 and 65 $\mathrm{ml\,s^{-1}}$ using a Cole-Parmer EW-03216-14 correlated flowmeter with valve. Flexible plastic 5 mm diameter PVC pipes connected the pump to the flowmeter and the flowmeter to the bolt at the back of the square support.

2.2. Fluid Rheology

The stress tensor τ is defined in terms of the shear rate tensor $\dot{\gamma}$ and the dynamic viscosity μ:

$$\tau_{ij} = \mu\,\dot{\gamma}_{ij}\;. \tag{1}$$

The shear rate $\dot{\gamma}$ is defined in terms of derivatives of the Eulerian velocity field $\mathbf{u}$:

$$\dot{\gamma}_{ij} = \partial_i u_j + \partial_j u_i\;. \tag{2}$$

Sludge rheology is complex. It displays non-Newtonian characteristics such as shear thinning, yield stress and shear banding (Baudez et al., 2013). Moreover, it often contains sand, cellulosic fibres and other debris, and therefore can be subject to sedimentation. However, the first approximation of considering the sludge as a power-law fluid with no sedimentation occurring proved to work well in a broad set of literature (e.g., Terashima et al. 2009; Bridgeman 2012; Wu 2014). In a power-law fluid the viscosity is not a constant, but depends on the shear rate magnitude $|\dot{\gamma}|$:

$$\mu = K\,|\dot{\gamma}|^{n-1} \ , \tag{3}$$

where K is the consistency coefficient (Pa s^n) and n is the power law index. In the case of the sludge we have $n < 1$, that is a pseudoplastic fluid. Here $|\dot{\gamma}|$ is defined as follows:

$$|\dot{\gamma}| = \frac{1}{\sqrt{2}}\sqrt{\dot{\gamma}_{ij}\,\dot{\gamma}_{ij}} \ . \tag{4}$$

Equation 3 holds only for an interval $(|\dot{\gamma}|_{\min}\,,\,|\dot{\gamma}|_{\max})$ (Wu and Chen, 2008; Bridgeman, 2012). Beyond that interval, the viscosity takes a constant maximum or minimum value. The values of $\mu_{\min}$ and $\mu_{\max}$ do not have physical meaning and are necessary to avoid singular values for the viscosity during the runs as well as to avoid unnecessary iterations. These values were chosen in a way that the maximum and minimum viscosity are comprised inside the interval $(|\dot{\gamma}|_{\min}\,,\,|\dot{\gamma}|_{\max})$ once stationary conditions had been reached. During the simulation runs, the value of μ is evaluated from Equation 2, Equation 4 according to the limitations on $|\dot{\gamma}|$ described above, and Equation 3, for every point $\mathbf{r}$ and time t. The field $\mu(\mathbf{r},\,t)$ thus obtained is used as an input to compute the velocity field.

Achkari-Begdouri and Goodrich (1992) investigated dairy cattle manure, and stated that the rheologic characteristics of the sludge depend on the total solid ratio (TS) and the temperature. Wu and Chen (2008) used their data as a basis for modelling sludge. These data are reported in Table 1 where the sludge densities for different TS are shown. All the values of density differ by less than 1% from water density at 35 degrees (994 kg/m3). For the sake of simplicity, in the CFD simulations a constant density of 1,000 $\mathrm{kg\,m^{-3}}$ was assumed.

[Table 2 about here.]

2.3. Preparation of the Liquid Phase

In the work reported here, water solutions of Sigma-Aldrich 419338 sodium carboxymetyl cellulose (CMC) with average molar weight of 700,000 were used in order to reproduce the behaviour of sludge. CMC is polymeric cellulose derivative that is widely used for reproducing pseudoplastic fluids, and, in particular, sludges (e.g. Wu and Chen (2008)). It consists of a white powder that can be dissolved into water and gives rise to a transparent solution. Three CMC solutions were employed, namely 2, 4 and 8 $\mathrm{g\,l^{-1}}$.

Each solution was prepared in the following way. (*i*) 5 litres of room temperature, tap water were poured into a bucket. (*ii*) A 20 cm width, 4 cm height rectangular impeller was used to stir the water. The impeller angular velocity was set in order to guarantee a sufficient degree of mixing, but to minimise the inclusion of air bubbles into the water. (*iii*) The CMC powder was added to the water at a rate not greater than 5 g $\mathrm{min^{-1}}$. (*iv*) The impeller mixed the solutions for between one and two hours, whereupon it was removed and the bucket sealed. The solution was left standing at room temperature for at least 24 hours.

Once filled with the CMC solutions, the wet height of the tank was 13 cm.

2.4. Rheological Measurements

Sludge rheology was assessed using a TA Instruments AR1000 rheometer fitted with a 40 mm diameter 2° steel cone.

Viscosity measurements were performed in the shear rate interval 100—500 s^{-1} and fitted to the power-law relation of Equation 3. The results are shown in Figure 2, and rheological data are reported in Table 2. The power-law assumption is clearly verified.

[Figure 2 about here.]

[Table 3 about here.]

2.5. Particle Image Velocimetry and High Speed Camera

PIV measurements were performed using a TSI PIV system (TSI Inc, USA). The system comprised a 532 nm (green) Nd-Yag laser (New Wave Solo III) pulsing at 7 Hz, synchronized to a single TSI Power view 4MP (2048 x 2048 pixels) 12 bit CCD camera using a synchronizer (TSI 610035) attached to a personal computer. The PIV system was controlled using TSI Insight 4G software. The spatial resolution of the measurements was 977 μm pixel^{-1}. Insight software was used to process the sets of pair raw images and convert them in a $n\times4$ matrix, where n is the number of cell of the grid and the four columns are x position, y position, x velocity and y velocity. Each experiment captured 300 images which were used to determine the average flow field of the system. The cell size for these experiments was chosen to be 64×64 pixels. Bubble size characterisation was undertaken using a Photron FASTCAM SA3. This camera had a CMOS sensor which provided mega pixel resolution (1K by 1K pixels) up to 2,000 frames per second (fps). The captured images were processed using ImageJ, a public domain software for images editing, for determining the bubble size. Evaluations of bubble diameters and regime velocity were obtained from visual examination of the outcome of the High Speed Camera experiment. If N is the number of bubbles crossing a given ideal horizontal plane in a time t and Q is the volume flow rate, then the average bubble volume can be evaluated by:

$$V_p = \frac{Qt}{N}\,, \tag{5}$$

and the diameter as:

$$d = \left(\frac{6}{\pi}V_p\right)^{1/3}\,. \tag{6}$$

Three CMC solutions were used (Section 2.3, Table 2) and for each of them, three different air flow rates were assessed. The values of Q, together with the measured quantities t and N and the resulting d are displayed in Table 3.

[Table 4 about here.]

The PIV technique detects the components of the Eulerian velocity field lying onto a given planar section of the fluid domain. A vertical plane, 3 cm away from the cylinder axis and parallel to the x axis was chosen for the scope:

$$\begin{cases} x \in (-X_{\max},\, X_{\max}) \\ y \in (0,\, H) \\ z = Z_{\mathrm{PIV}} \end{cases} \tag{7}$$

Here Z_{PIV} is the (constant) z coordinate at the PIV plane, $X_{\max} = (R^2 - Z_{\mathrm{PIV}}^2)^{1/2}$, where R is the tank radius, and H is the tank height. This plane is referred to as the PIV plane hereafter.

Experiments were performed for each of the CMC solutions shown in Table 2, and each of the air flow rates shown in Table 3. Once the regime conditions for the flow and the bubbly motion had been reached (at least 2 minutes after the air flow rate had been set), the average field was measured over a time period of approximately 3 s (being approximately the time between one bubble to reach the surface and the next one to do the same). The maximum experiment timescale was observed to be 0.34 s, which is one order of magnitude smaller than the PIV averaging time.

2.6. Average shear rate

The shear rate affects the bacteria populations involved into wastewater process (Gray, 2010)), and therefore average shear rate is a parameter of interest in environmental engineering design (Tchobanoglous et al., 2010). This approach is still in use, even if it has been pointed out (Camp and Stein, 1943; Clark, 1985) that a single number cannot represent a complex turbulent flow, in which areas of high input power coexist with dead zones (Sindall et al., 2013). Bridgeman (2012) performed CFD simulations on an impelled-stirred labscale digester and divided the domain into high, medium and low-velocity zones depending on the pointwise value of the velocity magnitude, and showed that a change in the impeller angular velocity does not affect the low-velocity zone relevantly.

Similarly, the shear rate value is expected to encompass several orders of magnitude due to coexistence of turbulent (around the bubbles) and relatively quiescent zones (Figure 5). Therefore it is appropriate to divide the domain into zones and compute the average shear rate therein. The purpose of the present work is to provide numerical validation for a CFD model, and therefore an analysis as in Bridgeman (2012) is out of scope. Nevertheless, it is fruitful to divide the domain into fixed, concentric zones, thus taking advantage of the axial symmetry, and compute the average shear rate therein. In this way, a single number can be associated to a relatively homogeneous zone, and then confronted with an analogous number calculated from the PIV data. This approach is simple as it uses only single numbers, but it is more meaningful than assessing simulated and experimental shear rate values averaged over the whole domain. This because, if the datum of the shear rate averaged is over the whole domain, an element of granularity would be lost.

Assuming axis symmetry, Equation 4 reduces to:

$$|\dot{\gamma}(r,\, y)| = \left| \frac{\partial u_r}{\partial y} + \frac{\partial u_y}{\partial r} \right| \,, \tag{8}$$

where r is the radial coordinate, and the tangential components of the shear stress are suppressed due to the radial symmetry. Equation 8 can be rewritten in terms of x and y, and thus evaluated on the PIV plane:

$$|\dot{\gamma}(x,\, y)| = \sqrt{1 + \frac{Z_{\mathrm{PIV}}^2}{x^2}} \left| \frac{\partial u_x}{\partial y} + \frac{\partial u_y}{\partial x} \right| . \tag{9}$$

The equation above can be discretized with a central differencing scheme. The intervals $(-X_{\max},\, X_{\max})$ and $(0,\, H)$ can be decomposed into $2N_x$ and N_y parts:

$$\begin{aligned} -X_{\max} \equiv x_{-N_x},\, x_{-N_x+1},\, \ldots,\, x_\alpha,\, \ldots,\, x_{N_x-1},\, x_{N_x} \equiv X_{\max} \\ 0,\, \ldots,\, y_\beta,\, \ldots,\, y_{N_y} \equiv H \end{aligned} \tag{10}$$

Then we have:

$$\begin{aligned} |\dot{\gamma}|_{\alpha\beta} \approx \sqrt{1 + \frac{Z_{\mathrm{PIV}}^2}{x_\alpha^2}} \Bigg| & \frac{u_{x,\,\alpha,\,\beta+1} - u_{x,\,\alpha,\,\beta-1}}{y_{\beta+1} - y_{\beta-1}} \\ & + \frac{u_{y,\,\alpha+1,\,\beta} - u_{y,\,\alpha-1,\,\beta}}{x_{\alpha+1} - x_{\alpha-1}} \Bigg| \,. \end{aligned} \tag{11}$$

The shear rate can be integrated over a volume domain comprised between two radii r_a and r_b and height equal to the cylinder wet height, and divided by the volume of the domain. This gives the average shear rate over that domain. r_a and r_b can be rewritten as $(x_a^2 + z^2)^{1/2}$ and $(x_b^2 + z^2)^{1/2}$ respectively, where x_a and x_b are the x components of r_a and r_b respectively. A change of integration variables from r to x thus allows us to express the average shear rate in tems of x and y, and to evaluate it by integrating over the PIV plane. x_a and x_b can be rewritten as $aX_{\max}$ and $bX_{\max}$:

$$\langle\dot{\gamma}\rangle_a^b = \frac{2}{X_{\max}^2 H\left(b^2 - a^2\right)} \int_0^H \mathrm{d}y \\ \frac{1}{2}\left(\int_{-bX_{\max}}^{-aX_{\max}} + \int_{aX_{\max}}^{bX_{\max}}\right) \mathrm{d}x\, \sqrt{x^2 + Z_{\mathrm{PIV}}^2}\; |\dot{\gamma}(x,\, y)|\ . \tag{12}$$

The expression above can be evaluated numerically with the rectangle rule method:

$$\langle\dot{\gamma}\rangle_a^b \approx \frac{2}{X_{\max}^2 H\left(b^2 - a^2\right)} \sum_{\beta=0}^{N_y} \frac{1}{2}\left(\sum_{\alpha=-b}^{-a} + \sum_{\alpha=a}^{b}\right) \\ \frac{x_{\alpha+1} - x_{\alpha-1}}{2}\, \frac{y_{\beta+1} - y_{\beta-1}}{2} \sqrt{x_\alpha^2 + Z_{\mathrm{PIV}}^2}\; |\dot{\gamma}|_{\alpha\beta}\ , \tag{13}$$

3. CFD

3.1. Model strategy

According to Andersson et al. (2012), an Euler-Lagrange (EL) model is preferable for multiphase modelling, provided that the number of particles is not so high as to render the computational cost prohibitive, and Sungkorn et al. (2011) employed the Euler-Lagrange model to simulate a bubble column rising in a Newtonian liquid. Sungkorn et al. (2012) subsequently employed the same model to simulate the motion of gas bubbles inside a non-Newtonian fluid mixed by a stirrer. The work reported in this paper followed this approach, and an Euler-Lagrange model in which the liquid and bubble phase are coupled together was employed.

In a full-scale plant, the bubbles rise in vertical columns the diameter of which is small compared with the digester size. Therefore, the focus of the work reported here was on resolving the flow patterns away from the bubble plume rather than describing the bubble motion in detail. For this reason, the following approximations were adopted: *(i)* bubble-bubble interactions were neglected; *(ii)* effects on fluid motion due to deformations of the bubble surface were neglected—this is equivalent to considering the bubbles to be spherical; *(iii)* bubbles were considered to be pointwise. These approximations do not allow a detailed description of the flow in close proximity to the bubbles, but do reproduce an interphase momentum transfer sufficiently accurate to reproduce the flow patterns away from the bubble column satisfactorily.

3.2. Liquid phase

In the EL model, the Navier-Stokes equations for the continuous phase are solved in conjunction with the equations of motion of the individual particles (Andersson et al., 2012). This coupling is realized by adding a momentum-transfer term to the equation. Thus the Navier-Stokes equations become:

$$\nabla \cdot \mathbf{u} = 0 \; ; \tag{14}$$

$$\rho \, \partial_t \mathbf{u} + \rho \nabla \cdot (\mathbf{u} \otimes \mathbf{u}) = -\nabla p + \nabla \cdot \tau + \rho \mathbf{g} + \mathbf{F} \; , \tag{15}$$

The viscosity τ has been defined in Equation 1. The term $\mathbf{F}$ is due to momentum exchange between fluid and particles. Further details on this term are explained in Section 3.3.

3.3. Bubble phase

The term $\mathbf{F}$ in Eq. 15 represents the momentum transfer between the fluid phase and each individual bubble (van Wachem and Almstedt, 2003) and can be expressed as follows:

$$\mathbf{F}(\mathbf{x}) = \sum_p \mathbf{F}_p \, \delta(\mathbf{x} - \mathbf{x}_p) \;\; , \tag{16}$$

where $\mathbf{F}_p$ is the resultant of the forces acting on the p-th bubble. The Dirac delta, after discretization, states that the contribution of the p-th bubble to Eq. 15 is $\mathbf{F}_p$ in the cell in which the bubble is present, and zero elsewhere. The equation of motion for each bubble is Newton's second law:

$$m_p \dot{\mathbf{u}}_p = \mathbf{F}_p \ , \tag{17}$$

where $\mathbf{u}_p \equiv \dot{\mathbf{x}}_p$ is the instantaneous velocity of the bubble. The resultant for the p-th bubble can be expressed as in Deen et al. (2004)

$$\mathbf{F}_p = \mathbf{F}_p^{\mathrm{a}} + \mathbf{F}_p^{\mathrm{b}} + \mathbf{F}_p^{\mathrm{d}} + \mathbf{F}_p^{\ell} \ , \tag{18}$$

that is: added mass, pressure gradient, buoyancy, drag, lift. We have:

$$\mathbf{F}_p^{\mathrm{a}} = C_{\mathrm{a}}\, \rho V_p \left(D_t \mathbf{u} - \mathrm{d}_t \mathbf{u}_p \right) \ , \tag{19}$$

$$\mathbf{F}_p^{\mathrm{b}} = V_p \left(\rho_p - \rho \right) \mathbf{g} \ , \tag{20}$$

$$\mathbf{F}_p^{\mathrm{d}} = \frac{1}{2} C_{\mathrm{d}}\, \rho\, \pi \frac{{d_p}^2}{4} \left| \mathbf{u} - \mathbf{u}_p \right| \left(\mathbf{u} - \mathbf{u}_p \right) \ , \tag{21}$$

$$\mathbf{F}_p^{\ell} = C_\ell\, \rho V_p \left(\mathbf{u} - \mathbf{u}_p \right) \wedge \nabla \wedge \mathbf{u} \ . \tag{22}$$

Here D_t indicates the total temporal derivative and reads $D_t \equiv \partial_t + \mathbf{u} \cdot \nabla$. The coefficients C_{a} and C_ℓ can be expressed as in the model proposed by Dewsbury et al. (1999), that is specific for gas bubbles and light solid particles rising in pseudoplastic liquids, and Tomiyama et al. (2002):

$$C_{\mathrm{a}} = \frac{1}{2} \ , \tag{23}$$

$$C_\ell = \begin{cases} \min\left[0.288\tanh\left(0.121\mathrm{Re}_p\right)\,, \; f(\mathrm{Eo}_d)\right]\,, & \mathrm{Re}_p \le 4\,, \\ f(\mathrm{Eo}_d)\,, & 4 < \mathrm{Re}_p \le 10\,, \\ -0.29\,, & \mathrm{Re}_p > 10\,, \end{cases} \tag{24}$$

where:

$$f(\mathrm{Eo}_d) = 0.00105\mathrm{Eo}_d{}^3 - 0.0159\mathrm{Eo}_d{}^2 - 0.0204\mathrm{Eo}_d + 0.474\,. \tag{25}$$

Eo_d is the modified Eötvös number and is defined as $(\rho_p - \rho)\, d_{d,p}{}^2/\sigma$, where $d_{d,p}$ is the maximum horizontal dimension of the p-th bubble. Since here the bubbles are considered to be spherical, $d_{d,p}$ is the bubble diameter. C_d is a function of the bubble Reynolds number (Dewsbury et al., 1999):

$$C_\mathrm{d} = \begin{cases} \dfrac{16}{\mathrm{Re}_p}\left(1 + 0.173\mathrm{Re}_p{}^{0.657}\right) + \dfrac{0.413}{1 + 16,300\mathrm{Re}_p{}^{-1.09}}\,, & \mathrm{Re}_p \le 195\,, \\ 0.95\,, & \mathrm{Re}_p > 195\,. \end{cases} \tag{26}$$

The bubble Reynolds number Re_p is defined as:

$$\mathrm{Re}_p = \frac{\rho\, d\, U_t}{\mu}\,, \tag{27}$$

where U_t is the velocity scale and is evaluated as the modulus of the difference between the bubble velocity and the fluid velocity in the bubble surroundings. During the simulation runs, the value of Re_p is evaluated from Equation 27 and the value of μ calculated is described in Section 2.2, for every point $\mathbf{r}$ and time t. The field $\mathrm{Re}_p(\mathbf{r}, t)$ thus obtained is used as an input to compute the velocity field.

3.4. Mesh

Each simulation was run in parallel on three dual-processor 8-core 64-bit 2.2 GHz Intel Sandy Bridge E5-2660 worker nodes with 32 GB of memory, for a total of 48 nodes. Six grids were generated for this study all with different cell numbers, but with the same structure. Details of the grids are summarised in Table 4, and an example is shown in Figure 3.

[Table 5 about here.]

[Figure 3 about here.]

The presence of a central column of bigger cells (Figure 3) is noteworthy. The bubble diameter is approximately 7 to 13 mm (cfr. Table 3). Thus, any mesh that can successfully reproduce the dynamics of this system should be formed by cells much smaller than a single bubble. However, this contradicts the assumption made earlier, that the bubbles are pointwise, and, more generally, a requirement for an Euler-Lagrange simulation that states that the parcel size should be much smaller than the cell size (van Wachem and Almstedt, 2003; Andersson et al., 2012). However, recent research (Sungkorn et al., 2011, 2012) demonstrated that this requirement can be relaxed if the number of bubbles remains "small". In the research cited above, the number of bubbles present in the system was of the order of $O(10^4)$ and therefore, the term "small" can be intended as "smaller than 10^4". It should be noted that that in Sungkorn et al. (2011, 2012) the continuous liquid phase was modelled using the lattice-Boltzmann method; that is not the case in the work reported here. However, the considerations above refer to the discrete bubble phase, the modelling of which is independent from the continuous phase. Therefore, it is appropriate to adopt the considerations of Sungkorn et al. (2011, 2012) for the bubble phase as valid also for the present work.

Nevertheless, it was observed in this study that the flow patterns depend strongly on the grid size when cells are much smaller than the bubbles. For this reason, larger cells, of the order of magnitude of the bubbles' volumes or slightly larger, were placed along the bubbles' expected trajectory.

Regarding the simulation of bubble injection, during the simulation, a bubble is "created" at certain times, in a place near the bottom of the tank, such that its centre lies along the cylinder axis, at about 5 to 11 mm from the bottom, and its velocity is zero. The reality is somewhat different, as a bubble takes non-zero time to expand out of the nozzle and then detaches with a non-zero velocity. The expansion of a bubble pushes upwards the water column above it; this may give rise to a liquid recall from the external zones near the bottom towards the centre in the lower part of the tank, and to an increase of the velocity of the liquid phase around the column above it. Both these possible effects are neglected in the model.

The liquid motion arises from momentum transfer from bubbles to liquid. As the bubbles are expected to form a vertical plume, it is reasonable to suppose that the turbulent Reynolds stress tensor R is not isotropic. Of the Reynolds stress models, the Launder-Reece-Rodi model takes into account both slow and rapid pressure strain terms of the Reynolds tensor, and it is the first that has been widely used (Pope, 2000). The Launder-Gibson model (Gibson and Launder, 1978), in addition to the former, takes into account the redistribution of normal stresses near the walls (ANSYS, 2012). It was considered that the wall effects may be of interest in the present study, and therefore the latter model was chosen.

The timestep was defined indirectly and dynamically by an algorithm aimed at keeping the maximum Courant number just below a specified limit of 0.2. The Courant number is a quantity defined for every cell such that given a cell labelled i, let be $|\mathbf{u}_i|$ the velocity magnitude, L_i the length dimension along $\mathbf{u}_i$ and Δt the timestep, then the Courant number for the cell i is:

$$\mathrm{Co}_i = \frac{|\mathbf{u}_i|\ \Delta t}{L_i}\ . \tag{28}$$

The maximum Courant number, Co, is the maximum value of Co_i over i. Starting from a small initial timestep (in this work, 10^{-5} s) the timestep was assessed in order to keep the maximum Courant number as near as possible to, but smaller than, the limit value of 0.2.

The initial conditions are reported in Table 5.

[Table 6 about here.]

Initially, a series of (transient) first-order runs was performed to simulate the development of the bubble column from a state in which no liquid phase motion and no bubbles were present in the system. As the object of study in this work is the liquid phase motion in presence of a fully-developed bubble column, the sole use of these first series of runs was to provide the initial conditions for the main (transient) second-order runs. The latter provided the data relative to the behaviour of the system in the presence of the fully-developed bubble column, and were compared with the experimental data.

The boundary conditions for the preliminary runs are shown in Table 5. The initial conditions for the preliminary runs were: $4.95\ 10^{-4}\ \mathrm{m}^2\,\mathrm{s}^{-3}$ for the ε field; zero for the other fields (p, u, R). The differencing schemes were: linear for interpolations, limited central differencing for the Gradient operator, linear for the Laplacian, Van Leer for all the other spatial operators. For the preliminary runs, the first-order Eulerian scheme for the time derivative was used; however, for the main runs, the second-order backward scheme was used.

CFD runs were performed for each of the CMC solutions as in Table 2, and each of the air flow rates of Table 3. The CFD output consists of a series of binary files arranged into directories, one for each timestep recorded. Binary files were collected for times corresponding to integer seconds after the initial conditions. The preliminary runs were performed for a simulation time of 10 s; then, their final timesteps were used as initial conditions for the main simulations, which were run for an additional simulation time of 50 s, for a total time of 60 s.

The binary files were processed to extract data to be compared with the PIV data. The Eulerian velocity field was interpolated onto the PIV plane. Then, the components parallel to the plane were averaged over time. As only the flow pattern originating from a fully-developed bubble column is of interest in this work, the preliminary times were not included into the average. Also the first ten seconds of the main runs were disregarded in order to avoid the artificial transience from first-order to second-order solutions. Thus, only the last (second-ordered) 40 seconds of each run were included in the average.

Despite the increase of the number of equations to be solved due to the choice of a Reynolds-stress turbulence model, the computational expense remained acceptable as the runtime remained below 30 hours per run. The timestep was observed to be between 0.0004 to 0.02 s. The number of bubbles present in the system at a given time was always less than 20 in all the runs. This kind of model is the ideal approach for dispersed phase systems (Andersson et al., 2012), and undoubtedly this model has benefitted from the small number of bubbles in terms of reduced computational expense compared with other options.

3.5. Impact of Central Cells Size

[Figure 4 about here.]

A preliminary series of runs was performed in order to verify that the flow patterns were stable under variations of the central cells size. The configuration labelled as cmc04-2 in Table 3 was tested with the Grids 4a, 4 and 4b described in Table 4 and the outcome is shown in Figure 4. The graphs show the magnitude of the velocity along three vertical lines lying on the PIV plane, respectively at 0.4, 0.6 and 0.8 half-widths from the central axis projection. There is a general good agreement between the three grids: small differences are either inside experimental errors (r/R=0.8 and r/R=0.6), or are confined to limited domain zones, such as near the surface, around the central axis (r/R-0.4 and, less, r/R=0.6).

3.6. Dependence from the mesh size

The Grid Convergence Index (GCI) proposed by Roache (1998) has become a standard method for assessing the independence of the CFD results from the mesh size and determining a measure of the error. According with Celik et al. (2008), a variable ϕ critical to the conclusions of the work is determined from three sets of grids, say a, b and c from the finest to the coarsest. The underlying hypothesis is that the value of ϕ determined by the simulation can be written as a Taylor polynomial (not necessarily infinite; therefore the Taylor polynomial may not be a Taylor series) of the grid spacing h:

$$\phi = \phi_{\text{exact}} + g_1 h + g_2 h^2 + g_3 h^3 + \dots \tag{29}$$

The apparent order of convergence p is calculated recursively in the following way:

$$\begin{aligned} p &= \frac{1}{\ln r_{ba}} \left| \ln \left| \varepsilon_{cb}/\varepsilon_{ba} \right| + p(q) \right| \\ q(p) &= \ln \frac{r_{ba}^{p} - s}{r_{cb}^{p} - s} \\ s &= \operatorname{sign}\left(\varepsilon_{cb}/\varepsilon_{ba}\right) \end{aligned} \tag{30}$$

where r_{cb} and r_{ba} are the linear refinement factors from mesh c to b and from mesh b to mesh a respectively, and:

$$\varepsilon_{cb} \equiv \phi_c - \phi_b \ , \qquad \varepsilon_{ba} \equiv \phi_b - \phi_a \ . \tag{31}$$

The grid convergence index (GCI) is defined as:

$$\mathrm{GCI}_{cb} \equiv \frac{1.25 \left| \varepsilon_{cb}/\phi_b \right|}{r_{cb} - 1} \ , \qquad \mathrm{GCI}_{ba} \equiv \frac{1.25 \left| \varepsilon_{ba}/\phi_b \right|}{r_{ba} - 1} \ . \tag{32}$$

The simulations are in the asymptotic range of convergence (and hence mesh independence is achieved) when

$$\frac{\mathrm{GCI}_{cb}}{r_{ba}^{p}\, \mathrm{GCI}_{ba}} \simeq 1 \ . \tag{33}$$

Under these circumstances, the value of GCI_{ba} can be used as a (conservative) estimation of the relative error on the finest mesh.

4. Results and discussion

The main runs comprised nine series, one for each of the configurations described in Table 2. In each series, the Grids 1, 2, 3 and 4 described in Table 4 were tested.

4.1. Assessment of the mesh dependence

A GCI analysis was carried out as described in Section 3.6. As the critical variable, the average shear rate over the whole computational domain was chosen. Two tests were performed for each run series, one involving grids 1,2 and 3, and another one involving grids 2, 3 and 4. The results are shown in Tables 6, 7 and 8.

[Table 7 about here.]

[Table 8 about here.]

[Table 9 about here.]

In most of the runs, the asymptotic convergence is reached for grid 2, but lost in grid 1. Oscillations are reported in the run series cmc02-2 and cmc04-2, with grid 1 behaving slightly better than grid 2 for the former series, and the converse for the latter. For the runs cmc04-1 and cmc04-3 the situation is less clear.

This behaviour is to be expected because, as explained in Section 3.4, there is a lower limit for the mesh size, dependant on the bubble size. Therefore, the GCI underlying hypothesis Equation 29 does not hold. Consequently, it is expected that the critical variable converges to, or oscillates around, a limit value for decreasing values of h, but still larger than the lower limit. Below this limit, the simulation is expected to produce unphysical results, and therefore the asymptotic convergence is lost.

The GCI test gives an indication whether the mesh is fine enough to achieve the asymptotic convergence range. However, in this context, it can give additional information about whether the mesh is too fine if compared with the bubble size. It can be concluded that the grid 1 is too fine, and that the grid 2 is optimal for all the runs except for the series cmc02-2, where the grid 1 is superior.

4.2. Analysis of the Velocity Field

Figure 5 shows a series of comparisons between PIV outcome and simulation, for the example cases labelled as cmc02-2, cmc04-2 and cmc08-2. Grid 1 was used in all the cases. The simulations reproduce well the measured flow both in magnitude and in flow shape. Also the position of the centre of the vortices correlates well with the PIV outcome. The principal differences between simulation and PIV consist of: *(i)* under-estimated velocity magnitude around the bubble column, especially at the bottom; *(ii)* slightly over-estimated velocity in the upper part of the tank; and *(iii)* slightly under-estimated velocity in the lower part of the tank.

[Figure 5 about here.]

Examination of Figure 5 indicates that (i) is the most significant difference. In this regard, it should be noted that the bubble column was interposed between the PIV plane and the camera. Therefore, there is a refraction effect of the laser rays through the bubbles and thus the PIV data may be less robust in the inner parts of the domain. As an example of this, by a simple application of the Snell's law with standard values for the refraction coefficients of air (1.000) and water (1.333), it can be noted that a laser beam scattering into a bubble with an impact parameter of half the bubble radius is deflected of an angle of 20.5°. Nevertheless, explanations concerning the nature and the approximations of the theoretical model can be elaborated. In particular:

(i) for under-estimation of velocity magnitude there are three possible causes. First, the cells along the central column are much larger than any other cell, and there are only 10 to 12 along the whole tank height (see Table 4). Thus, there may be too few cells to expect an accurate description of the flow near the central axis. The second source of error may be related to the way the parcels are introduced into the system.

The implications of this simplification, in particular regarding the possible increase of liquid phase velocity in the central column, have been discussed in Section 3.4. A final cause for this difference may be the fact that, due to the assumption made in Section 3.1, the model may simply be unable to reproduce the flow in the immediate surroundings of a bubble.

For *(ii)* the cause of over-estimation of velocity in the upper part of the tanks may lie in the description of the liquid-atmosphere interface. It was observed that the bubble column gives rise to a water hump just above it, and to vertical oscillations along the whole interface. This phenomenon is more evident when the viscosity decreases (Figure 6). The fraction of the bubbles' kinetic energy that is transferred to the liquid phase is then redistributed as kinetic energy and potential energy of the mass displaced into the hump, and also to the air above due to the interface oscillations. In the simulations, however, the interface is modelled as a rigid non-slip surface, and no liquid displacement is possible, nor is any energy transfer to the air. The transferred energy is therefore not redistributed, and remains in the form of liquid kinetic energy. Thus, the simulations over-estimate the velocity field magnitude especially in the regions where the energy redistribution should (but does not) take place, i.e. near the interface or just below it.

[Figure 6 about here.]

In the case of *(iii)* as before, velocity under-estimation in the lower part of the tank may once again be due to the way the bubbles are introduced into the system. The implications of this simplification, in particular with regard to the possible liquid recall from the external zones, have been discussed in Section 3.4.

All runs' outcomes are displayed in Figure 7 (2 $\mathrm{g\,l^{-1}}$ solution), Figure 8 (4 $\mathrm{g\,l^{-1}}$ solution) and Figure 9 (8 $\mathrm{g\,l^{-1}}$ solution). The graphs show the magnitude of the projected velocity along three vertical lines lying on the PIV plane, respectively at 0.4, 0.6 and 0.8 half-widths from the central axis projection, as shown in Figure 4. The runs were carried out with Grids 1,2,3 and 4. There is a good general agreement between the different grids. In particular, the differences are smaller when the CMC concentration increases. The runs with larger mesh size (especially Grid 4) sporadically differ in the lower concentrations, in particular in the $2\ \mathrm{g\,l^{-1}}$. In general, the experimental data are well reproduced by the computational runs. Only the local minima on the r/R=0.4 runs are not very well reproduced. This corresponds to a slight misplacement of the main vortices towards the central axis, as can also be noted in Figure 5. The effect is more marked when the CMC concentration increases. Nevertheless, the agreement, even quantitatively, is good.

[Figure 7 about here.]

[Figure 8 about here.]

[Figure 9 about here.]

4.3. Average Shear Rate calculation

Figure 10 depicts the average shear rate over different domains. It is evident that the major discrepancies between experimental and simulated data are concentrated in the inner part of the domain—between 0 and $0.2X_{\mathrm{max}}$, and, to a lesser extent, between $0.2X_{\mathrm{max}}$ and $0.5X_{\mathrm{max}}$. As expected, there is no agreement between computational and PIV data between 0 and $0.2X_{\mathrm{max}}$, for the reasons discussed above. However, the agreement is good in the external part of the domain, between $0.5X_{\mathrm{max}}$ and X_{max}. This result can be considered satisfactory because it provides a further confirmation that the CFD model presented in this work is able to reproduce the flow patterns in the zone of interest for the anaerobic digestion design, that is, away from the bubble column.

Interestingly, the average shear rate values are comprised between 0.1 and 1 s^{-1}, well below the value of 50-80 s^{-1} suggested by literature for anaerobic digestion plants (Tchobanoglous et al., 2010). Similarly, low values of shear rate magnitude compared with the literature were found also in Bridgeman (2012), where it was observed that the presence of dead or low-mixed zones could not be avoided even by increasing the power input, and that this fact did not affect the biogas production.

[Figure 10 about here.]

5. Conclusions

A novel EL model for gas-mixing in anaerobic digestion was developed.

The model was validated with lab-scale data, under the most adverse circumstances—that is, bubble sizes not negligible when compared with cells sizes. The relative simplicity of the viscosity model did not affect the results of the simulations. It would be interesting to test more complex viscosity models in future works. The design of the solver facilitates the addition of other types of Lagrangian particles; and this aspect may be used to introduce sedimenting particles.

Care must be adopted in choosing the appropriate mesh resolution. In particular, a mesh that is too fine may be detrimental for mesh independence; for this reason, a mesh independence test such as GCI is essential.

Because of the refraction of the laser rays through the gas bubbles, the PIV technique can give unreliable results in the regions near the bubble column. The fact that the flow away from the bubble column is satisfactorily reproduced suggests that the bubble-liquid phase momentum transfer is modelled with a sufficient degree of accuracy, but further research with different experimental techniques is desirable to measure the flow in the regions near the bubble column.

In conclusion, in the zones of interest for purposes of full-scale simulations, the model reproduces the experimental data robustly and with fidelity. Therefore, it can be successfully employed for full-scale predictions.

Acknowledgements

The computational work reported in this paper was undertaken using the BlueBEAR high performance computing facility at the University of Birmingham, UK. The authors are grateful for the facility and support provided by the University.
The laboratory work was undertaken under the supervision of Prof Mark Simmons; his contribution is gratefully acknowledged.
The first author is funded via a University of Birmingham Postgraduate Teaching Assistantship award.

References

Achkari-Begdouri, A., Goodrich, P.R., 1992. Rheological properties of dairy cattle manure. Bioresour. Technol. 40, 149–156. doi:10.1016/j.biortech.2004.06.020.

Andersson, B., Andersson, R., Hå kansson, L., Mortensen, M., Defence, N., Sudiyo, R., van Wachem, B., 2012. Computational Fluid Dynamics for Engineers. Cambridge University Press.

ANSYS, 2012. ANSYS FLUENT 14.5 Theory Guide. ANSYS, Inc.

Baudez, J.C., Slatter, P., Eshtiaghi, N., 2013. The rheological behabiour of anaerobic digested sludge. Chem. Eng. J. 215-216, 182–187. URL: http://dx.doi.org/10.1016/j.watres.2011.08.035, doi:10.1016/j.cej.2012.10.099.

Bridgeman, J., 2012. Computational fluid dynamics modelling of sewage sludge mixing in an anaerobic digester. Adv. Eng. Softw. 44, 54–62. URL: http://dx.doi.org/10.1016/j.advengsoft.2011.05.037, doi:10.1016/j.advengsoft.2011.05.037.

Camp, T.R., Stein, P.C., 1943. Velocity gradients and internal work in fluid motion. J. Bost. Soc. Civ. Eng. 85, 218–237.

Celik, I.B., Ghia, U., Roache, P.J., Freitas, C.J., Coleman, H., Raad, P.E., 2008. Procedure for Estimation and Reporting of Uncertainty Due to Discretization in CFD Applications. J. Fluids Eng. 130, 078001. doi:10.1115/1.2960953.

Clark, M.M., 1985. Critique of Camp and Stein's RMS velocity gradient. J. Environ. Eng. I, 741–754.

Deen, N.G., van Sint Annaland, M., Kuipers, J.A.M., 2004. Multi-scale modeling of dispersed gas-liquid two-phase flow. Chem. Eng. Sci. 59, 1853–1861. doi:10.1016/j.ces.2004.01.038.

Dewsbury, K., Karamanev, D., Margaritis, a., 1999. Hydrodynamic characteristics of free rise of light solid particles and gas bubbles in non-Newtonian liquids. Chem. Eng. Sci. 54, 4825–4830. doi:10.1016/S0009-2509(99)00200-6.

Gibson, M.M., Launder, B.E., 1978. Ground effects on pressure fluctuations in the atmospheric boundary layer. J. Fluid Mech. 86, 491–511. doi:10.1017/S0022112078001251.

Gómez, X., Cuetos, M.J., Cara, J., Morán, a., García, a.I., 2006. Anaerobic co-digestion of primary sludge and the fruit and vegetable fraction of the municipal solid wastes. Conditions for mixing and evaluation of the organic loading rate. Renew. Energy 31, 2017–2024. doi:10.1016/j.renene.2005.09.029.

Gray, N.F., 2010. Water Technology: An Introduction for Environmental Scientists and Engineers. IWA Publishing. doi:10.1016/B978-1-85617-705-4.00026-5.

Karim, K., Thoma, G.J., Al-Dahhan, M.H., 2007. Gas-lift digester configuration effects on mixing effectiveness. Water Res. 41, 3051–3060. doi:10.1016/j.watres.2007.03.042.

McMahon, K.D., Stroot, P.G., Mackie, R.I., Raskin, L., 2001. Anaerobic codigestion of municipal solid waste and biosolids under various mixing conditions-II: Microbial population dynamics. Water Res. 35, 1817–1827. doi:10.1016/S0043-1354(00)00438-3.

Ong, H.K., Greenfield, P.F., Pullammanappallil, P.C., 2002. Effect of mixing on biomethanation of cattle-manure slurry. Environ. Technol. 23, 1081–1090.

Pope, S.B., 2000. Turbulent Flows. Cambridge University Press.

Roache, P.J., 1998. Verification of codes and calculations. AIAA J. 36, 696–702. doi:10.2514/3.13882.

Sindall, R.C., Bridgeman, J., Carliell-Marquet, C., 2013. Velocity gradient as a tool to characterise the link between mixing and biogas production in anaerobic waste digesters. Water Sci. Technol. 67, 2800–2806. doi:10.2166/wst.2013.206.

Stroot, P.G., McMahon, K.D., Mackie, R.I., Raskin, L., 2001. Anaerobic codigestion of municipal solid waste and biosolids under various mixing conditions-I. digester performance. Water Res. 35, 1804–1816. doi:10.1016/S0043-1354(00)00439-5.

Succi, S., 2001. The Lattice Boltzmann Equation for Fluid for Fluid Dynamics and Beyond. doi:10.1016/0370-1573(92)90090-M.

Sungkorn, R., Derksen, J.J., Khinast, J.G., 2011. Modeling of turbulent gas-liquid bubbly flows using stochastic Lagrangian model and lattice-Boltzmann scheme. Chem. Eng. Sci. 66, 2745–2757. URL: http://dx.doi.org/10.1016/j.ces.2011.03.032, doi:10.1016/j.ces.2011.03.032.

Sungkorn, R., Derksen, J.J., Khinast, J.G., 2012. Modeling of aerated stirred tanks with shear-thinning power law liquids. Int. J. Heat Fluid Flow 36, 153–166. URL: http://dx.doi.org/10.1016/j.ijheatfluidflow.2012.04.006, doi:10.1016/j.ijheatfluidflow.2012.04.006.

Tchobanoglous, G., Burton, Franklin, L., Stensel, H.D., 2010. Wastewater Engineering. Metcalf & Eddy, Inc.

Terashima, M., Goel, R., Komatsu, K., Yasui, H., Takahashi, H., Li, Y.Y., Noike, T., 2009. CFD simulation of mixing in anaerobic digesters. Bioresour. Technol. 100, 2228–2233. URL: http://dx.doi.org/10.1016/j.biortech.2008.07.069, doi:10.1016/j.biortech.2008.07.069.

Tomiyama, A., Tamai, H., Zun, I., Hosokawa, S., 2002. Transverse migration of single bubbles in simple shear flows. Chem. Eng. Sci. 57, 1849–1858. doi:10.1016/S0009-2509(02)00085-4.

Versteeg, H.K., Malalasekera, W., 1995. An introduction to Computational Fluid Dynamics. Longman Scientific & Technical.

Vesvikar, M.S., Al-Dahhan, M.H., 2005. Flow pattern visualization in a mimic anaerobic digester using CFD. Biotechnol. Bioeng. 89, 719–732. doi:10.1002/bit.20388.

van Wachem, B.G.M., Almstedt, A.E., 2003. Methods for multiphase computational fluid dynamics. Chem. Eng. J. 96, 81–98. doi:10.1016/j.cej.2003.08.025.

Ward, A.J., Hobbs, P.J., Holliman, P.J., Jones, D.L., 2008. Optimisation of the anaerobic digestion of agricultural resources. Bioresour. Technol. 99, 7928–7940. doi:10.1016/j.biortech.2008.02.044.

Wolf-Gladrow, D., 2005. Lattice-Gas Cellular Automata and Lattice Boltzmann Models. Springer.

Wu, B., 2010. CFD simulation of gas and non-Newtonian fluid two-phase flow in anaerobic digesters. Water Res. 44, 3861–3874. URL: http://dx.doi.org/10.1016/j.watres.2010.04.043, doi:10.1016/j.watres.2010.04.043.

Wu, B., 2012. Integration of mixing, heat transfer, and biochemical reaction kinetics in anaerobic methane fermentation. Biotechnol. Bioeng. 109, 2864–2874. doi:10.1002/bit.24551.

Wu, B., 2014. CFD simulation of gas mixing in anaerobic digesters. Comput. Electron. Agric. 109, 278–286. URL: http://www.sciencedirect.com/science/article/pii/S0168169914002543, doi:10.1016/j.compag.2014.10.007.

Wu, B., Chen, S., 2008. CFD simulation of non-Newtonian fluid flow in anaerobic digesters. Biotechnol. Bioeng. 99, 700–711. doi:10.1002/bit.21613.

List of Figures

1 Experimental rig top and front view. Pump, flowmeter, pipes and fittings not shown. 34
2 Shear rate-shear stress dependance. Points: measured values. Lines: best fits. 35
3 Example of the grids described in Table 4. 36
4 Preliminary series along a vertical axis against PIV outcome. Red: Grid 4a. Blue: Grid 4. Green: Grid 4b. 37
5 Projected velocity plots using the Grid 1. cfd02-2: *(a)*: PIV outcome, *(b)*: CFD simulation. cfd04-2: *(c)*: PIV outcome, *(d)*: CFD simulation. cfd08-2: *(e)*: PIV outcome, *(f)*: CFD simulation. 38
6 Liquid-arir interface. *(a)*: cmc02-1. *(b)*: cmc02-2. *(c)*: cmc02-3. *(d)*: cmc04-1. *(e)*: cmc04-2. *(f)*: cmc04-3. *(g)*: cmc08-1. *(h)*: cmc08-2. *(i)*: cmc08-3. 39
7 CFD-simulated velocity magnitude along a vertical axis against PIV outcome. 2 $\mathrm{g\,l^{-1}}$. 40
8 CFD-simulated velocity magnitude along a vertical axis against PIV outcome. 4 $\mathrm{g\,l^{-1}}$. 41
9 CFD-simulated velocity magnitude along a vertical axis against PIV outcome. 8 $\mathrm{g\,l^{-1}}$. 42
10 Average shear rate over different subdomains: comparison between experimental and simulated data. Below: ratio between simulated and experimental data. 43

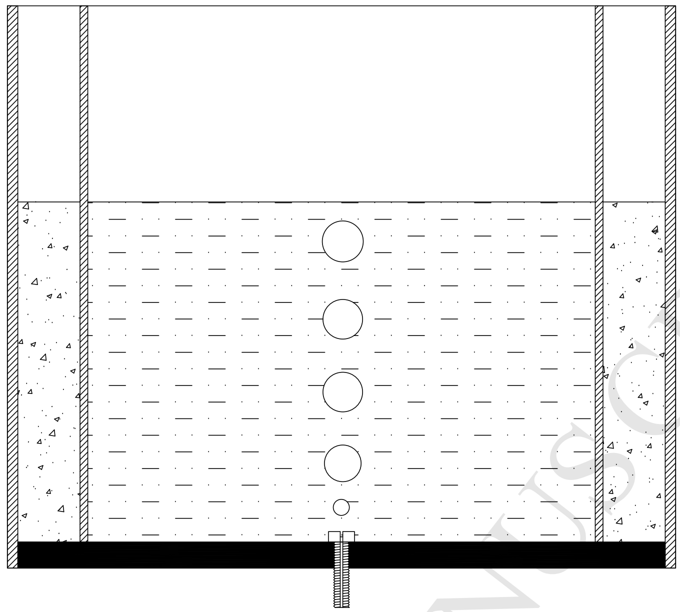

(a)

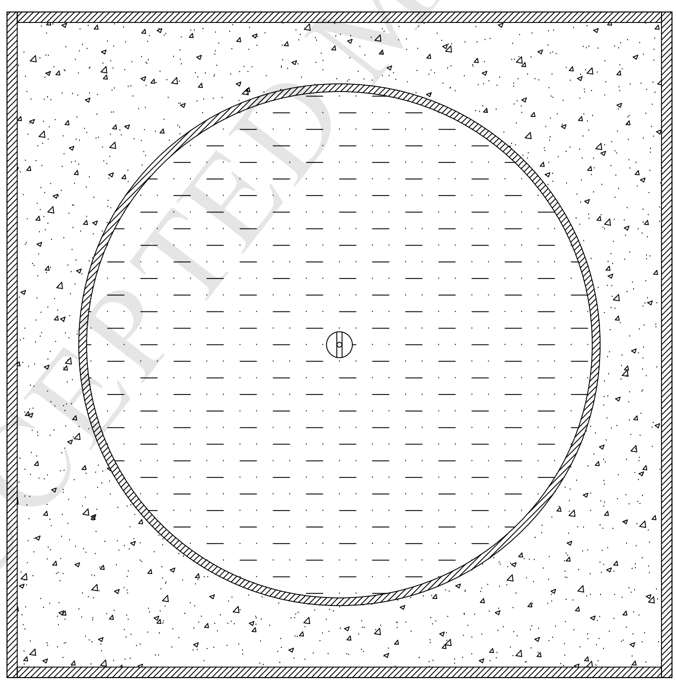

(b)

Figure 1 *Experimental rig top and front view. Pump, flowmeter, pipes and fittings not shown.*

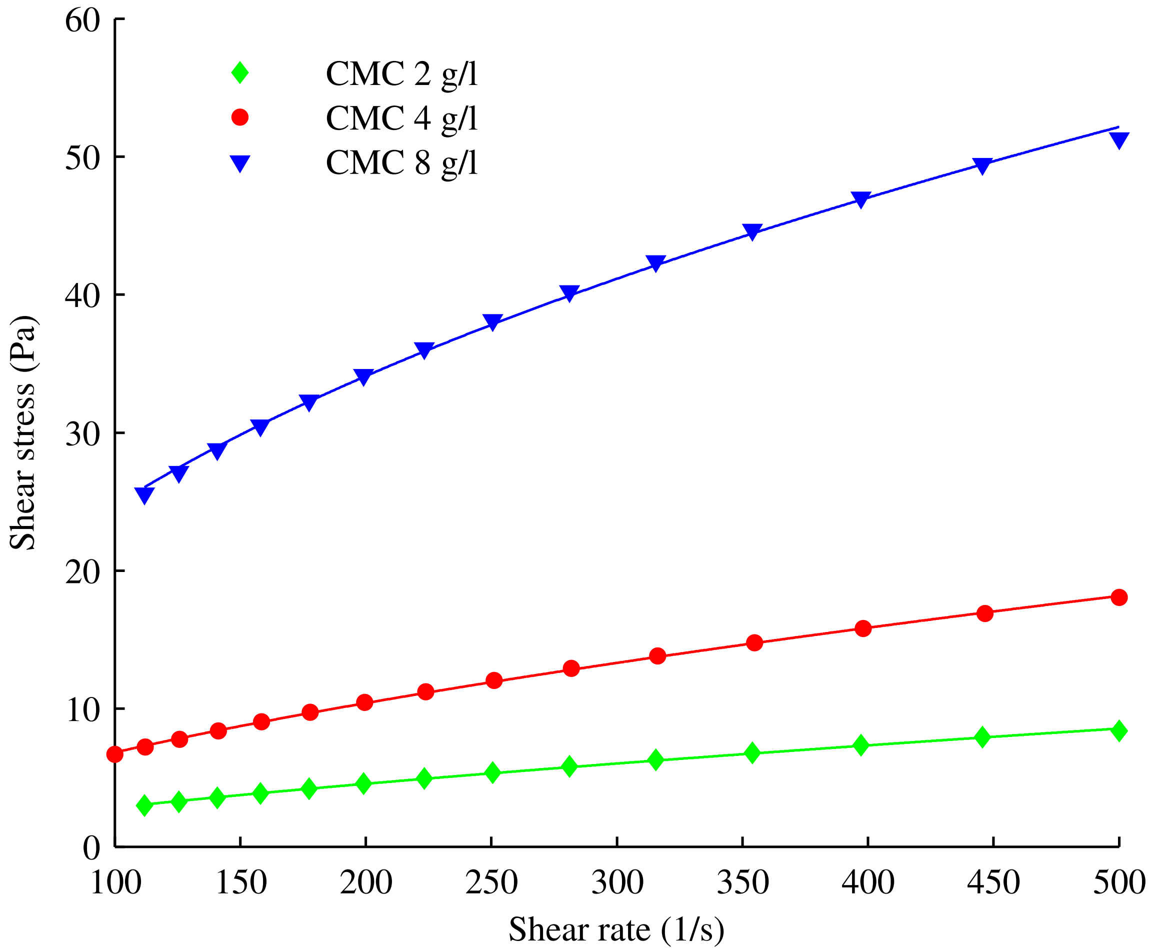

Figure 2 *Shear rate-shear stress dependance. Points: measured values. Lines: best fits.*

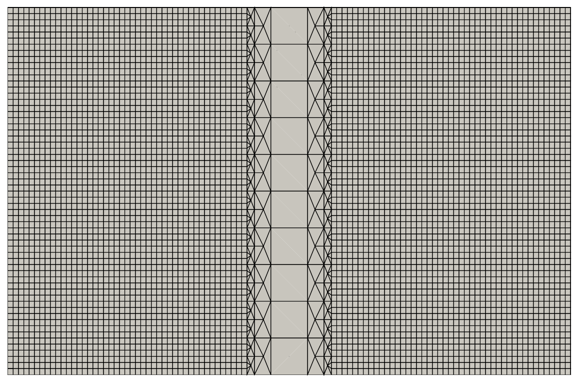

(a)

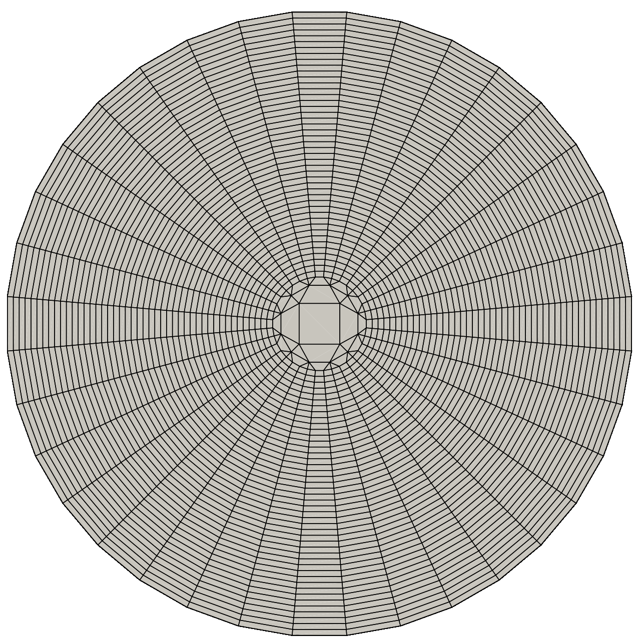

(b)

Figure 3 *Example of the grids described in Table 4.*

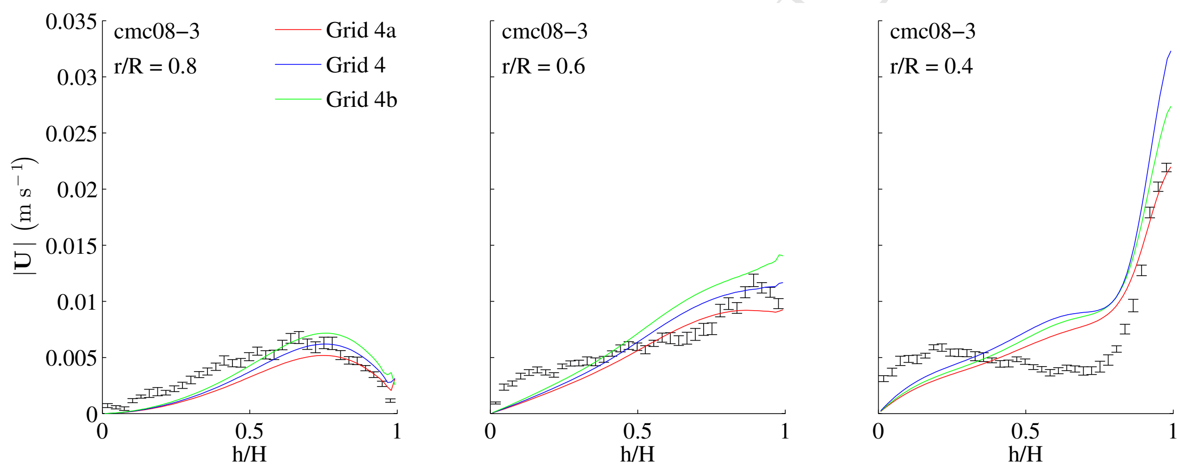

Figure 4 *Preliminary series along a vertical axis against PIV outcome. Red: Grid 4a. Blue: Grid 4. Green: Grid 4b.*

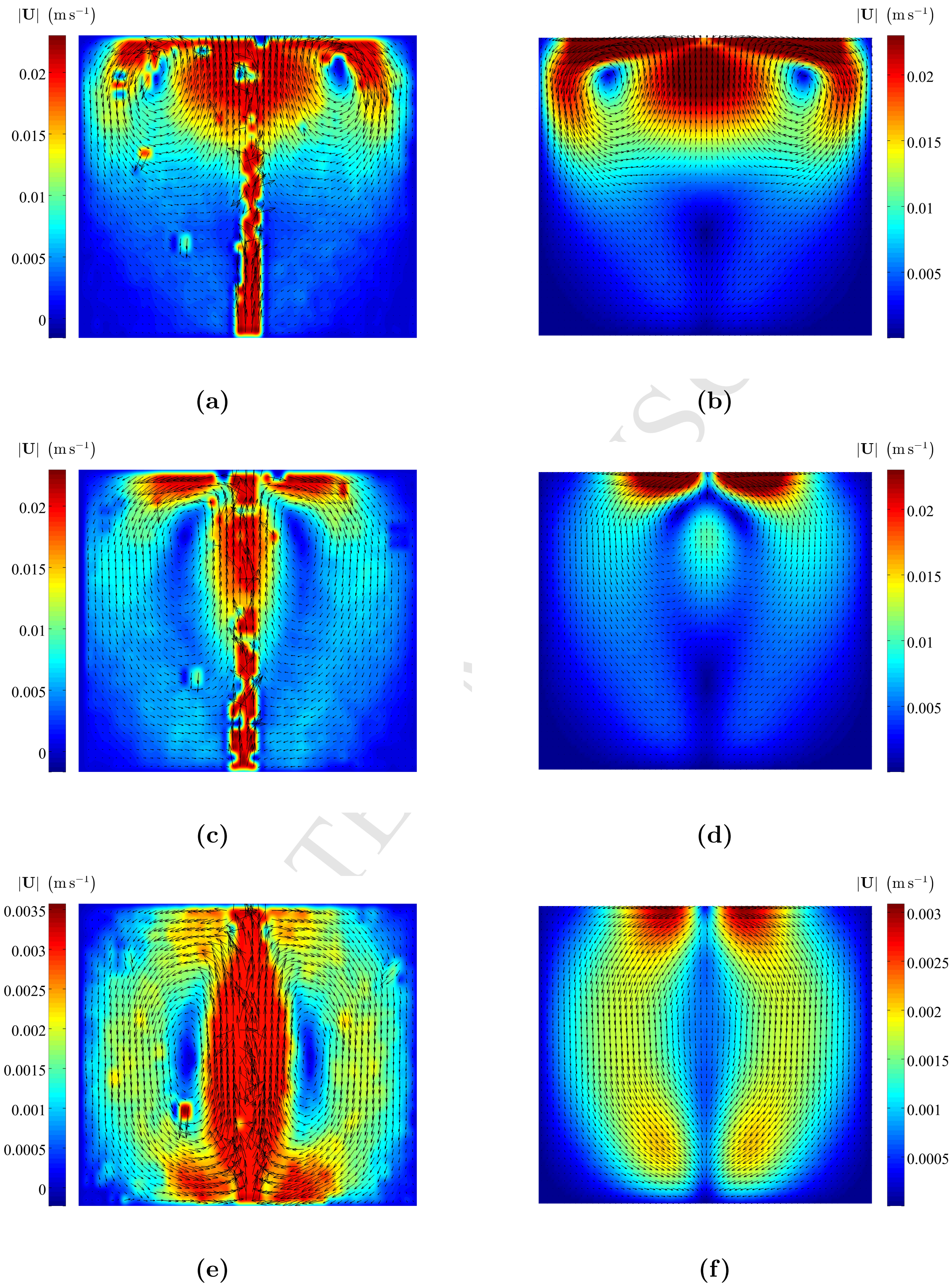

Figure 5 *Projected velocity plots using the Grid 1. cfd02-2:* (a)*: PIV outcome,* (b)*: CFD simulation. cfd04-2:* (c)*: PIV outcome,* (d)*: CFD simulation. cfd08-2:* (e)*: PIV outcome,* (f)*: CFD simulation.*

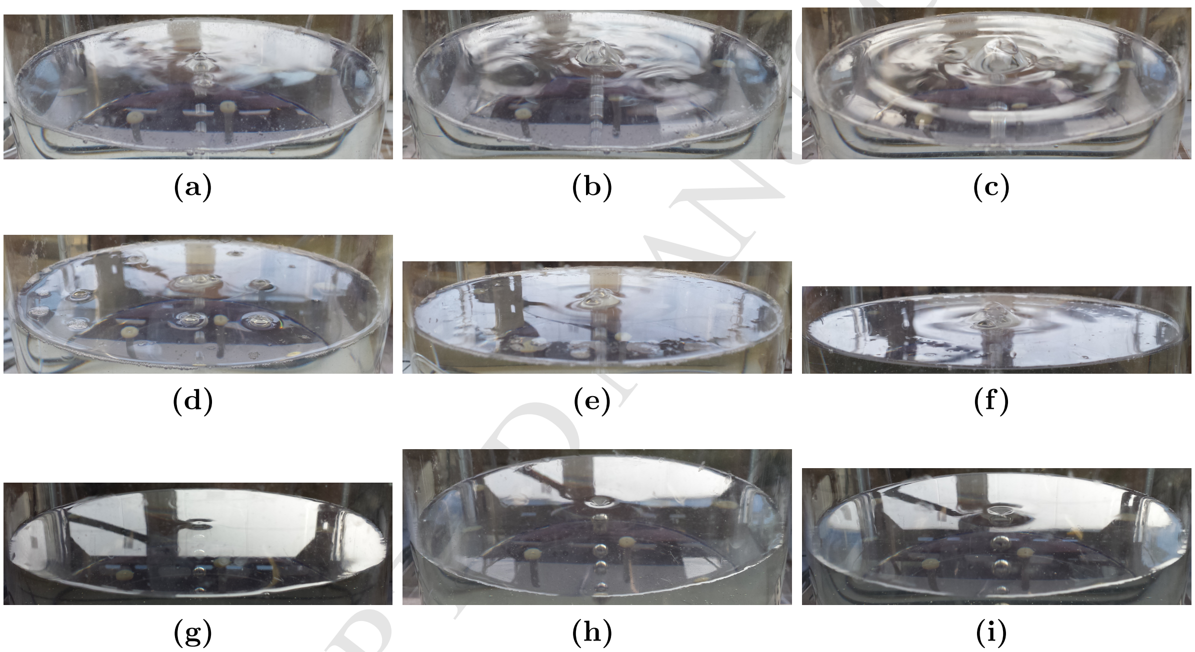

Figure 6 *Liquid-arir interface.* (a)*: cmc02-1.* (b)*: cmc02-2.* (c)*: cmc02-3.* (d)*: cmc04-1.* (e)*: cmc04-2.* (f)*: cmc04-3.* (g)*: cmc08-1.* (h)*: cmc08-2.* (i)*: cmc08-3.*

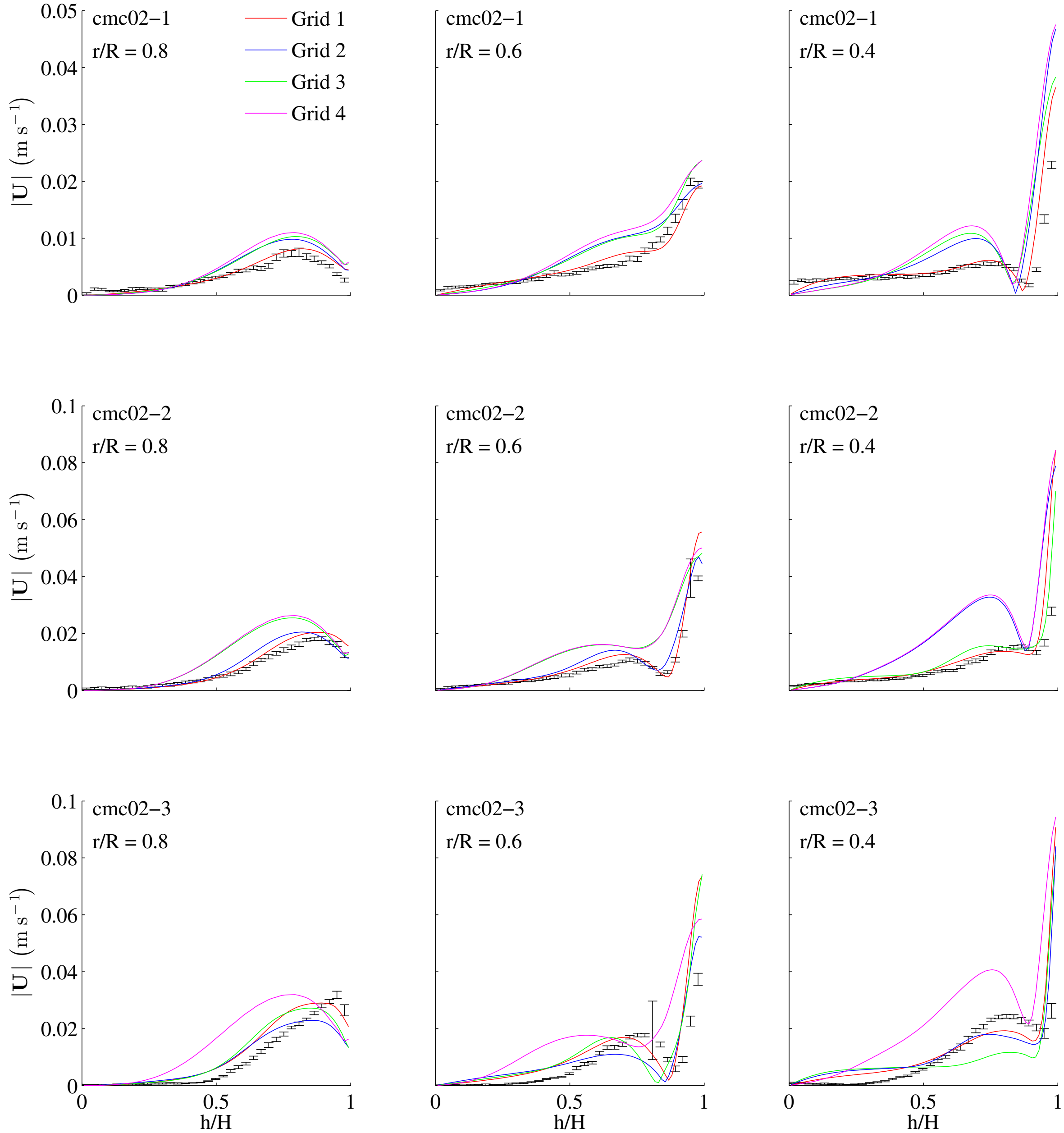

Figure 7 *CFD-simulated velocity magnitude along a vertical axis against PIV outcome. 2* $\mathrm{g\,l^{-1}}$.

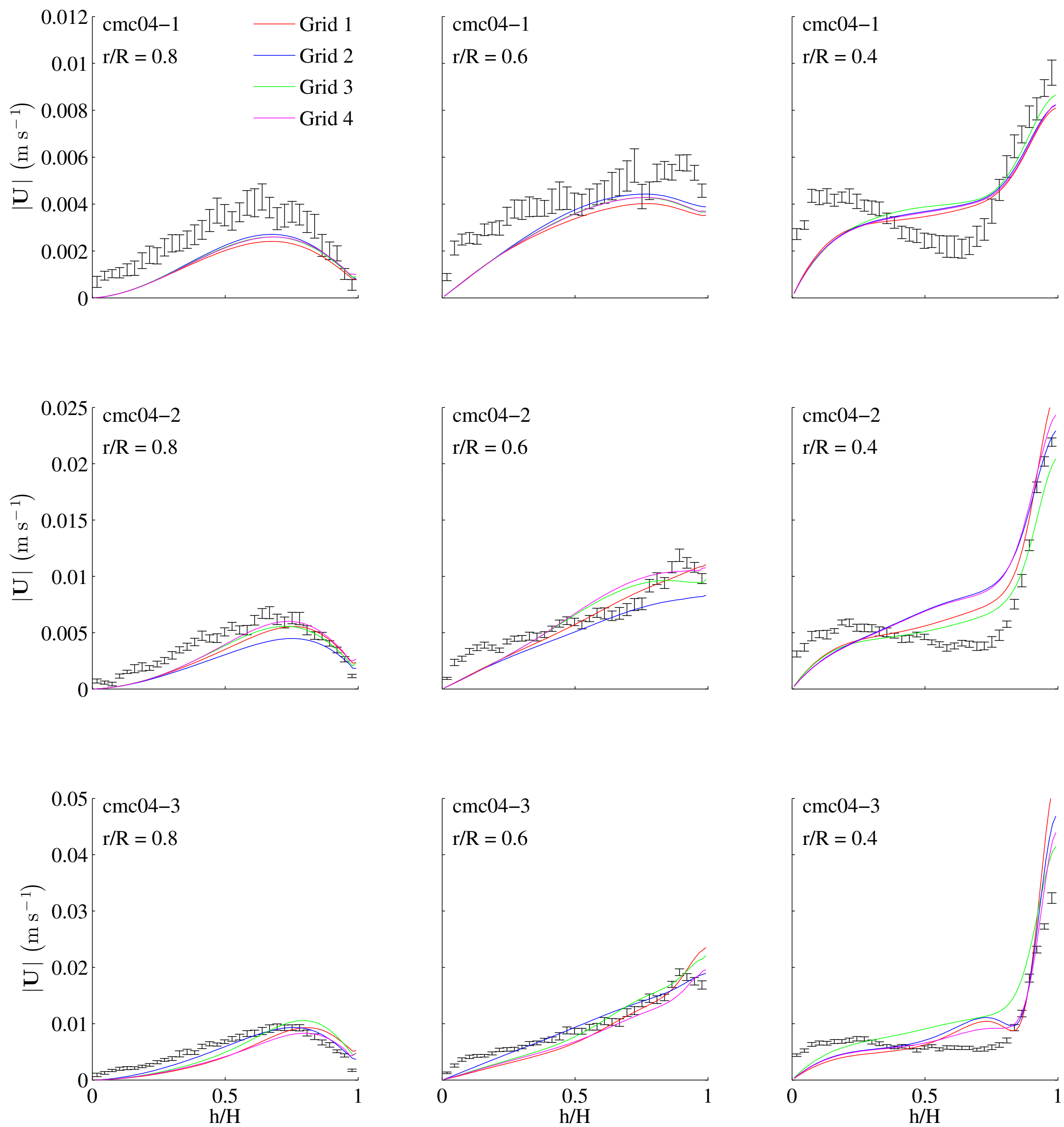

Figure 8 *CFD-simulated velocity magnitude along a vertical axis against PIV outcome. 4* $\mathrm{g\,l^{-1}}$.

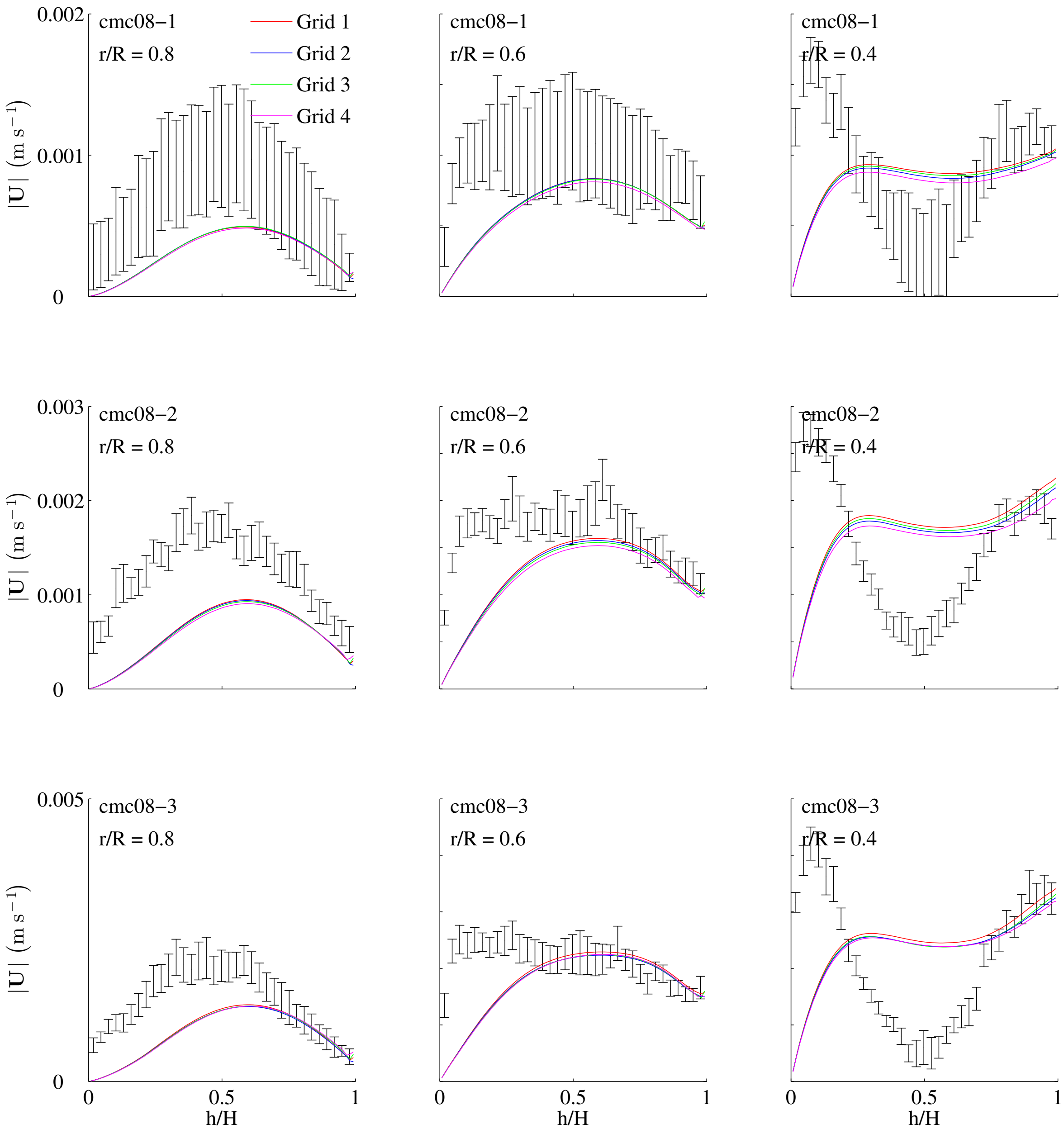

Figure 9 *CFD-simulated velocity magnitude along a vertical axis against PIV outcome. 8* g l^{-1}.

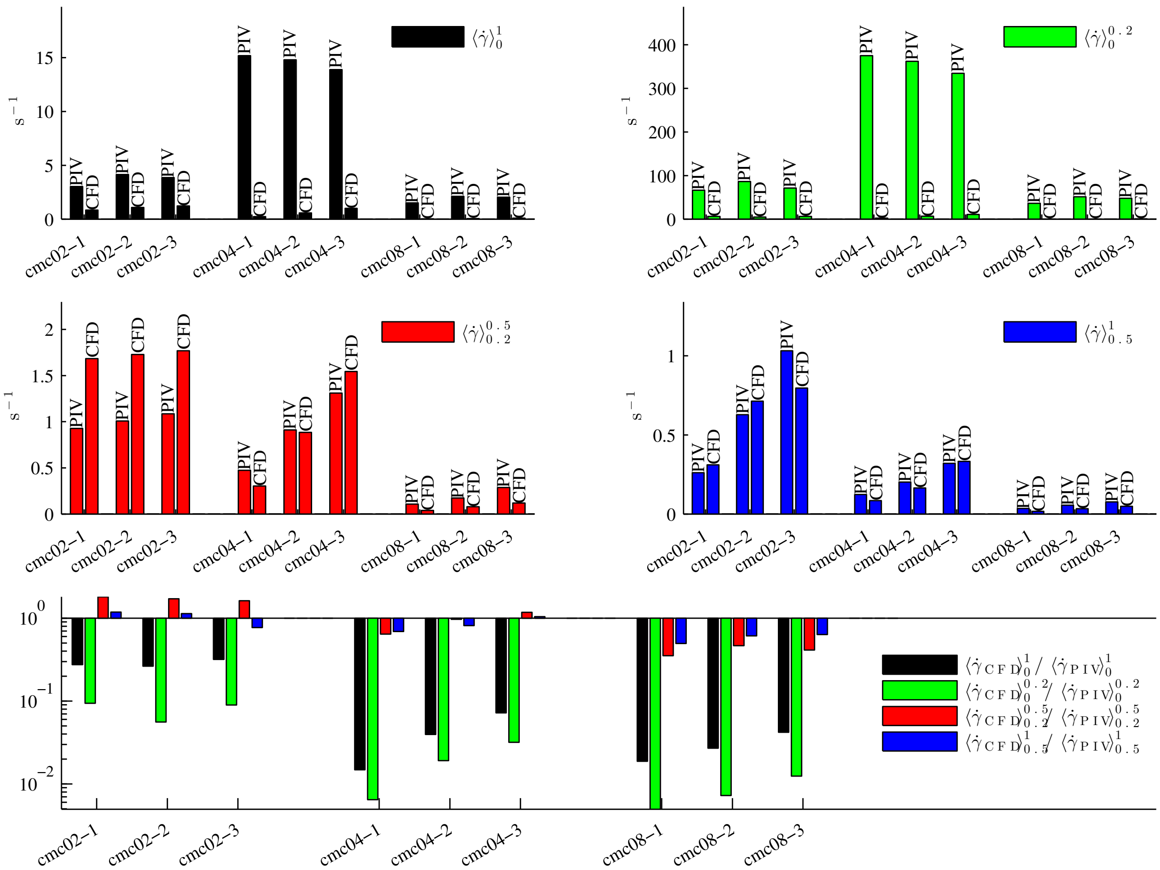

Figure 10 *Average shear rate over different subdomains: comparison between experimental and simulated data. Below: ratio between simulated and experimental data.*

List of Tables

1 Rheological properties of sludge at T=35 °C (from Achkari-Begdouri and Goodrich (1992)). . . . 46
2 Fitted parameters for the shear rate-shear stress dependance. . . . 47
3 High speed camera outcome. . . . 48
4 Details of the grids. . . . 49
5 Boundary and initial conditions. . . . 50
6 GCI analysis. 2 g l^{-1}. . . . 51
7 GCI analysis. 4 g l^{-1}. . . . 52
8 GCI analysis. 8 g l^{-1}. . . . 53

Nomenclature

$\dot{\gamma}$	Shear rate, s^{-1}
Co	Courant number
Eo	Modified Eötvös number
Re_p	Bubble Reynolds number
μ	Power law viscosity, Pa s
ρ	Liquid phase density, kg m^{-3}
τ	Shear stress, Pa
$\mathbf{g}$	Acceleration of gravity, m s^{-1}
$\mathbf{u}$	Liquid phase velocity field, m s^{-1}
$\mathbf{u}_p$	Velocity of the p-th bubble, m s^{-1}
d_p	Diameter of the p-th bubble, m
K	Consistency coefficient, Pa s^n
m_p	Mass of the p-th bubble, kg
n	Power law index
p	Pressure, Pa
V_p	Volume of the p-th bubble, m^3
CFD	Computational Fluid Dynamics
CMC	Carboxymethil cellulose
GCI	Grid Convergence Index
PIV	Particle Image Velocimetry

Table 1 *Rheological properties of sludge at T=35 °C (from Achkari-Begdouri and Goodrich (1992)).*

TS (%)	K (Pa s^n)	n (–)	$\lvert\dot{\gamma}\rvert$ range (s^{-1})	μ_{min} (Pa s)	μ_{max} (Pa s)	Density (kg m^{-3})
2.5	0.042	0.710	226—702	0.006	0.008	1,000.36
5.4	0.192	0.562	50—702	0.01	0.03	1,000.78
7.5	0.525	0.533	11—399	0.03	0.17	1,001.00
9.1	1.052	0.467	11—156	0.07	0.29	1,001.31
12.1	5.885	0.367	3—149	0.25	2.93	1,001.73

Table 2 *Fitted parameters for the shear rate-shear stress dependance.*

Label (−)	Concentration ($g\,l^{-1}$)	K ($Pa\,s^n$)	n (−)
cmc02-*	2	0.054	0.805
cmc04-*	4	0.209	0.730
cmc08-*	8	1.336	0.619

Table 3 *High speed camera outcome.*

Label (–)	Q ($\mathrm{ml\,s^{-1}}$)	d (mm)	Figures (–)
cmc02-1	2.05	7.01	7
cmc02-2	5.30	7.01	5a, 5b, 7
cmc02-3	8.63	7.01	7
cmc04-1	2.05	7.94	8
cmc04-2	5.30	7.94	5c, 5d, 8
cmc04-3	8.63	7.94	8
cmc08-1	2.05	11.0	9
cmc08-2	5.30	12.8	5e, 5f, 9
cmc08-3	8.63	13.8	9

Table 4 *Details of the grids.*

Grid Id.	Cells no.	Central cells size	Central cells no.	Cells over circle
1	2,348,787	9.19 mm	10	72
2	1,361,367	9.19 mm	10	60
3	230,410	9.19 mm	10	48
4a	121,240	7.66 mm	12	36
4	97,210	9.19 mm	10	36
4b	77,992	11.0 mm	8	36

Table 5 *Boundary and initial conditions.*

Place	Quantity	Condition
Top	p	Constant zero
	$\mathbf{u}$	Slip
	ε	Slip
	R_{ij}	Slip
Wall / bottom	p	Adjusted such that the velocity flux is zero
	$\mathbf{u}$	Constant zero
	ε	Wall function
	R_{ij}	Wall function

Table 6 *GCI analysis. 2 g* l^{-1}.

	cmc02-1	cmc02-2	cmc02-3
$\langle\dot{\gamma}\rangle_4$ (s^{-1})	0.9662	1.7051	1.9331
$\langle\dot{\gamma}\rangle_3$ (s^{-1})	0.8757	1.6717	1.4556
$\langle\dot{\gamma}\rangle_2$ (s^{-1})	0.8357	1.0916	1.2244
$\langle\dot{\gamma}\rangle_1$ (s^{-1})	0.6446	1.2838	1.5850
p_2	3.855	2.755	3.605
p_1	—	2.337	—
$GCI2_{43}$	$6.360\ 10^{-2}$	$2.065\ 10^{-2}$	$2.252\ 10^{-1}$
$GCI2_{32}$	$6.799\ 10^{-3}$	$1.616\ 10^{-1}$	$3.167\ 10^{-2}$
$GCI1_{32}$	—	$2.222\ 10^{-1}$	—
$GCI1_{21}$	—	$3.536\ 10^{-1}$	—
Asymp.2	0.954	0.025	0.841
Asymp.1	—	0.411	—

Table 7 *GCI analysis. 4 g* l^{-1}.

	cmc04-1	cmc04-2	cmc04-3
$\langle\dot{\gamma}\rangle_4$ (s^{-1})	0.2125	0.5358	0.8568
$\langle\dot{\gamma}\rangle_3$ (s^{-1})	0.2144	0.6393	0.8829
$\langle\dot{\gamma}\rangle_2$ (s^{-1})	0.2249	0.4586	0.9994
$\langle\dot{\gamma}\rangle_1$ (s^{-1})	0.2076	0.5866	1.3548
p_2	1.314	0.725	1.028
p_1	—	2.809	—
$\mathrm{GCI2}_{43}$	$2.397\ 10^{-2}$	$8.729\ 10^{-1}$	$1.071\ 10^{-1}$
$\mathrm{GCI2}_{32}$	$4.974\ 10^{-2}$	$9.185\ 10^{-1}$	$1.739\ 10^{-1}$
$\mathrm{GCI1}_{32}$	—	$1.152\ 10^{-1}$	—
$\mathrm{GCI1}_{21}$	—	$4.091\ 10^{-1}$	—
Asymp.2	0.221	0.619	0.335
Asymp.1	—	0.169	—

Table 8 *GCI analysis. 8 g* l^{-1}.

	cmc08-1	cmc08-2	cmc08-3
$\langle\dot{\gamma}\rangle_4$ (s^{-1})	0.0273	0.0549	0.0841
$\langle\dot{\gamma}\rangle_3$ (s^{-1})	0.0282	0.0570	0.0848
$\langle\dot{\gamma}\rangle_2$ (s^{-1})	0.0283	0.0573	0.0851
$\langle\dot{\gamma}\rangle_1$ (s^{-1})	0.0285	0.0582	0.0864
p_2	8.134	7.458	3.258
p_1	—	—	—
$\mathrm{GCI2}_{43}$	$4.272\ 10^{-3}$	$6.124\ 10^{-3}$	$6.089\ 10^{-3}$
$\mathrm{GCI2}_{32}$	$3.447\ 10^{-5}$	$7.365\ 10^{-5}$	$8.811\ 10^{-4}$
$\mathrm{GCI1}_{32}$	—	—	—
$\mathrm{GCI1}_{21}$	—	—	—
Asymp.2	1.003	1.005	1.004
Asymp.1	—	—	—

- A CFD model for gas mixing in anaerobic digestion is developed.
- We present the first Euler-Lagrange model for the scope.
- Motion arises by momentum transfer from bubbles to liquid phase.
- Lab-scale validation with PIV technique was carried out.
- The model reproduces well the experimental data.